*Journal of Metals, Materials and Minerals, 36(3), e2819, 2026*

# $Li_5FeO_4$ as a cathode prelithiation additive: Doping engineering and first-principles research

Zixiang LI[1,†], Zile ZOU[1,†], Jialan LI[1], Chennan MA[1], Jiarun LI[1], Xiaoyu LIU[2], Jin YI[2,*], and Jianhui LI[1,*]

[1] *School of Materials and New Energy, South China Normal University, Shanwei Guangdong, 516600, China*
[2] *Institute for Sustainable Energy/College of Sciences, Shanghai University, Shanghai, 200444,China*

***Corresponding author e-mail**: jin.yi@shu.edu.cn, Jianhuili@m.scnu.edu.cn
**†These authors contributed equally to this work**

**Received date:**
24 July 2026
**Revised date:**
5 August 2026
**Accepted date:**
14 August 2026

**Keywords:**
Lithium ion batteries;
Prelithiation;
$Li_5FeO_4$;
Doping;
First principles

**Abstract**

During the initial charge-discharge cycle, irreversible loss of active lithium (~ 5% to 15%) severely affects the battery energy density and shortens cycle life of lithium-ion batteries (LIBs). Prelithiation strategy has gradually become an effective approach to compensate for the irreversible loss of active lithium. Lithium ferrate ($Li_5FeO_4$, LFO) is considered to be a promising cathode prelithiation additive due to its high theoretical capacity (867 mAh·g$^{-1}$), suitable delithiation potential (3.5 V to 4.1 V), and competitive raw material. However, the application of LFO is limited by the its properties including poor air stability, low electronic conductivity, and incomplete delithiation. Currently, great efforts are made to address the above limitations through surface coating and bulk doping. This review summarizes the recent advances in Fe-site and non-Fe-site doping, highlighting the effects of dopants on modulating the crystal structure, $Li^+$ diffusion kinetics, and electrochemical properties of LFO. The studies of first-principles on doped LFO, including formation energies, density of states, and migration barriers together with the value of theoretical tools when assessing doping performance are presented. In the end, the remaining challenges and future development directions for LFO doping design are put forward, offering perspectives for advancing prelithiation strategy in high-energy-density LIBs.

## 1. Introduction

### 1.1 Background of prelithiation in lithium-ion batteries

Driven by the rapid expansion of new energy automobiles and electrochemical energy storage markets, LIBs are required urgently to deliver higher energy density and longer cycle lifespan [1–3]. Silicon-based anodes are regarded as the core material for breaking the current energy density bottleneck of LIBs, because its theoretical specific capacity (~4200 mAh·g$^{-1}$) far exceeding that of conventional graphite anodes (372 mAh·g$^{-1}$) [4]. Silicon expands its volume by more than 300% during the initial charge-discharge cycle, leading to repeated rupture and regeneration of the solid electrolyte interphase (SEI) [5]. Around 15% or more active lithium disappears permanently. The full-cell energy density decreases over 30% from its theoretical value, so that it severely hinders commercial application [6]. Prelithiation technology introduces additional active lithium sources into the cell system to compensate for lithium loss during SEI formation and subsequent cycling. It is the most effective strategy for enhancing energy density and cyclic stability of full cells. At present, this approach is primarily divided into two technical routes: anode prelithiation and cathode sacrificial additives [7]. Stabilized lithium metal powder (SLMP), lithium foil contact, and chemical prelithiation belongs to the anode prelithiation techniques, they indeed can achieve high lithium compensation efficiencies. Nevertheless, lithium metal is highly reactive. Factories must maintain harsh manufacturing conditions (dew point below –40°C) and adopt sophisticated equipment. The poor compatibility with existing LIB production lines is poor, further escalating the cost of large-scale production [8,9]. Cathode sacrificial additives are different. They can be blended into cathode slurries without modifying existing production lines. They possess superior safety and process compatibility, and gradually become the mainstream industrialization pathway [10]. Among mainstream cathode prelithiation additives, Although $Li_2NiO_2$ have a delithiation capacity of approximately 320 mAh·g$^{-1}$, it is highly reactive with ambient moisture to form insulating impurities such as LiOH and $Li_2CO_3$, and its cobalt content further increases raw material costs [11]. $Li_3N$ exhibits an extremely high theoretical delithiation capacity up to 2308 mAh·g$^{-1}$. Its decomposition potential is only ~0.9 V. It strongly reacts with moisture and cannot coexist with N-methylpyrrolidone (NMP), the regular solvent for cathode slurries, thereby large-scale production faces huge obstacles [12]. Different from the above two candidates, LFO boasts a theoretical delithiation capacity of 867 mAh· g$^{-1}$ and an actual usable capacity of approximately 700 mAh·g$^{-1}$. Its delithiation potentials are concentrated within the 3.5 V to 4.1 V range, perfectly matching the operational voltage window of existing LIBs. Moreover, LFO is derived from inexpensive iron-based raw materials without reliance on precious metals, making it fully compatible with current cathode manufacturing processes. Consequently, it stands out as the most promising sacrificial cathode prelithiation agent for industrial-scale applications [13,14].

### 1.2 Fundamental characteristics and bottlenecks of LFO

LFO crystallizes in the orthorhombic structure with Pnma space group, where $FeO_6$ octahedra are connected via share edges to form a three-dimensional framework, and $Li^+$ ions occupy the skeletal interstitial sites. This endows the materials with repaid ionic conduction along the b-axis. First-principles calculations indicate that its bandgap is approximately 2.3 eV to 2.8 eV, depending on the selection of Hubbard U correction. Therefore, LFO is classified as a wide-bandgap semiconductor. Because of this wide bandgap electronic structure, the electronic conductivity of material is limited. and it is difficult to efficiently achieve charge compensation during lithium removal. Thus, it is usual for people to use doping strategies to narrow the bandgap and enhance charge transfer kinetics of the delithiation process. Under this electronic structure framework, its delithiation process follows a cation/anion dual-redox mechanism: during the initial charge at a low-potential plateau (3.5 V), 2 $Li^+$ are extracted. This is accompanied by the oxidation of approximately 50% of $Fe^{3+}$ to $Fe^{4+}$ and the partial oxidation of $O^{2-}$ to $O^-$ and $O_2$. Consequently, the crystal structure transitions from an ordered orthorhombic phase to a disordered rock-salt phase, $Li_3FeO_{3.5}$. On the high-potential plateau at 4.0 V, two additional $Li^+$ are extracted, ultimately yielding amorphous $LiFeO_2$. This corresponds to a theoretical maximum delithiation of 4 mol $Li^+$ per mol of LFO, which corresponds to a capacity of 867 $mAh{\cdot}g^{-1}$ [13]. LFO works well as a lithium supplier. However, four major drawbacks slow down its industrial development:

(1) Poor air stability: Surface $Li^+$ reacts quickly with $CO_2$ and $H_2O$ from the surroundings. Insulating impurities, such as $Li_2CO_3$ and LiOH, are generated. After exposure to air for 24 h, it becomes more difficult to achieve exceeding 75% delithiation capacity loss of preparing cathode slurries [14].

(2) Low intrinsic ionic/electronic conductivity: The isolated $FeO_4$ tetrahedra is unfavorable to build continuous $Li^+$ diffusion channels, leading to the hindered electron transport and polarization effects with a decreased actual lithium utilization rate (below 80%).

(3) Active oxygen release during delithiation: The electrolyte oxidization will be take place due to the highly oxidative $O_2$ and $O^-$ species, resulting in the gas evolution, battery expansion, and higher internal resistance as well as the deteriorative safety and cycle life of LIBs [14].

(4) Severe lattice strain in delithiation: Micron single-crystal LFO particles would crack into polycrystalline nanoparticles, which results in to the increased interfacial resistance and the decayed lithium supplement effect [14].

### 1.3 Scope of this review

Different from previous reviews encompassing the comprehensive LFO modification strategies, this paper concentrates on the core control strategy of elemental doping for LFO following the coating and composite phase modifications as comparative references. Except for integrating doping mechanisms revealed by density functional theory (DFT) calculations, this review correlates the improved electrochemical performance (e.g., increased capacity and improved stability) with theoretical fundamental understanding as well, including electronic structure modulation, $Li^+$ diffusion barriers reduction, and lattice oxygen stability enhancement, which would present bidirectional validation between experimental observations and theoretical predictions. The presented prospects would provide theoretical guidance and technical supports for the industrial application of LFO.

## 2. Fundamental structure and delithiation mechanism of pristine LFO

### 2.1 Crystal structure and intrinsic electronic structure

The crystal structure of LFO belongs to orthorhombic anti-fluorite type and matches space group Pbca. The lattice parameters $a \approx 9.218$ Å, $b \approx 9.213$ Å, and $c \approx 9.153$ Å. The unit cell of this structure is about twice the size of cubic $Li_2O$ (Fm3m), which is because $Fe^{3+}$ orderly replaces for $Li^+$ in the sublattice [15]. Oxygen atoms are arranged in a face-centered cubic (fcc) close-packed lattice. 7/8 of the tetrahedral interstitial sites are filled by $Li^+$, while $Fe^{3+}$ replace an equivalent amount of three $Li^+$. The other half of the tetrahedral sites remain unoccupied. The formula $[Li_{1.25}Fe_{0.25}\square_{0.50}]O$ can be described this structure, where □ denotes intrinsic lithium vacancies. LFO exhibits a distinctive structural motif characterized, which is isolated $FeO_4$ tetrahedra. These tetrahedra are solely connected with adjacent $LiO_4$ tetrahedra through vertex-sharing, instead of forming the continuous Fe–O–Fe network commonly seen in layered transition metal oxides [16,17].

Natural defects exist in pure LFO, and lithium vacancies are not the only type. During the high-temperature solid-state synthesis process, which is the main preparation method for LFO, the evaporation of $Li_2O$ at elevated temperatures can induce the formation of oxygen vacancies and lead to non-stoichiometric components like $Li_5FeO_{4-\delta}$. These vacancies scatter charge carriers and further reduce the low intrinsic conductivity of LFO [17,18]. First-principles DFT calculations indicate that the valence band maximum (VBM) of LFO mainly comes from O 2p orbitals, and the conduction band minimum (CBM) is contributed by Fe 3d orbitals. The intrinsic band gap is approximately 4.0 eV, classifying LFO as a wide-bandgap insulator [16,19]. Its unique electronic structure leads to low electronic conductivity. Meanwhile, the isolated $FeO_4$ tetrahedra block the migration of lithium ions. $Li^+$ can only move between independent tetrahedral and octahedral interstitial sites. For this reason, the intrinsic ionic conductivity of LFO is merely $\sim 10^{-8}$ $S{\cdot}cm^{-1}$, which becomes a key obstacle to its high-rate application [15,16].

### 2.2 Electrochemical delithiation and relithiation mechanisms

The electrochemical delithiation process of LFO exhibits two obvious voltage plateaus. Its theoretical maximum extraction capacity is 4 mol $Li^+$ per mole of LFO, corresponding to a theoretical specific capacity of 867 $mAh{\cdot}g^{-1}$ [14,18]. The first low-voltage plateau at around 3.5 V (vs. $Li^+/Li$) corresponds to the extraction of 2 mol $Li^+$ ($Li_{5-x}FeO_4$, $x = 0$ to 2), where approximately 50% of $Fe^{3+}$ are oxidized to $Fe^{4+}$. It is the primary charge compensation mechanism and the oxidation state of O remains largely at –2. The ordered orthorhombic anti-fluorite phase gradually transforms into a disordered rock-salt phase $Li_3FeO_{3.5}$, driven by the migration of $Fe^{3+}$ from tetrahedral to octahedral interstitial sites [15,19]. The forward migration barrier for $Fe^{3+}$ is merely 0.25 eV according to First-principles DFT calculations,

which allows the process to happen spontaneously at ambient temperature. This low energy barrier explains why first-cycle activation in LFO is easily observed in experiments [16].

The second high-voltage plateau occurs at around 4.0 V (vs. $Li^+/Li$). It corresponds to the extraction of the remaining 2 mol of $Li^+$ ($Li_{3-x}FeO_{3.5-x/2}$, where x = 2 to 4). At this stage, the cationic redox capacity of $Fe^{3+}/Fe^{4+}$ is near saturation and charge compensation shifts to anionic redox. The oxide anion $O^{2-}$ undergoes oxidation to form $O^-$ and even neutral $O^0$ species as well. Meanwhile, a fraction of the lattice oxygen is released as $O_2$ gas. Figure 1 shows these voltage plateaus intuitively. Co doped LFO and LCO ($Li_6CoO_4$) have similar platform properties [20]. The final delithiation product is amorphous $LiFeO_2$, the overall reaction can be written as follows [21]:

$$Li_5FeO_4 \rightarrow 4Li^+ + 4e^- + O_2 + LiFeO_2 \quad (1)$$

Apart from the above changes, the diffusion pathways of $Li^+$ are intricately coupled with Fe migration. When $Li^+$ is extracted from the tetrahedral sites, the disappearance of electrostatic screening destabilizes the $FeO_4$ tetrahedra, which prompt $Fe^{3+}$ to occupy adjacent octahedral vacancies and further open $Li^+$ diffusion channels within the evolving disordered rock-salt phase[16,22].

The relithiation capability of LFO is decided by its irreversible first-cycle delithiation. During initial charge, the $Li^+$ extracted from LFO migrates to the anode, in order to compensate for the irreversible loss of active lithium caused by SEI growth, transition metal dissolution, and electrolyte decomposition on graphite/silicon-based anodes. After delithiation, the residual iron oxide phase remains electrochemically inert in the normal voltage window of LIBs. This avoid extra parasitic capacity output when LFO is used as a sacrificial relithiation agent. [18,23].

Recent applications in all-solid-state batteries have further demonstrated that the irreversible $Li^+$ release from LFO can effectively offset lithium consumption caused by interfacial side reactions between sulfide solid electrolytes and high-nickel cathodes, thereby significantly extending the cycle life of anode-free configurations [18].

## 2.3 Failure mechanism: Theoretical basis for doping modification

Three interrelated failure mechanisms dominate the performance degradation of pure-phase LFO, which provides clear targets for subsequent doping modification strategies.

### 2.3.1 Interfacial Side Reactions of Water Vapor/$CO_2$

The $Li^+$ on the LFO surface exhibits high chemical activity due to the low-coordination environment of surface O atoms. The DFT adsorption energy calculations confirm that the adsorption energies for $H_2O$ and $CO_2$ on the LFO (214) surface are –1.23 eV and –0.98 eV, respectively, which are thermodynamically highly prone to spontaneous interfacial reactions [17,24]:

$$Li_5FeO_4 + 2H_2O \rightarrow 4LiOH + LiFeO_2 \quad (2)$$

$$0.5Li_5FeO_4 + CO_2 \rightarrow Li_2CO_3 + 0.5LiFeO_2 \quad (3)$$

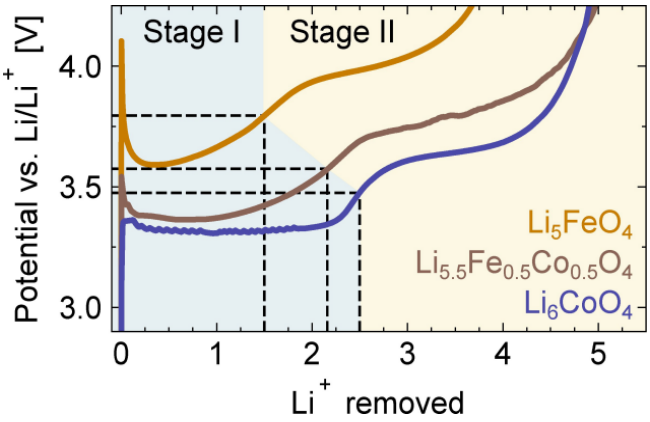


**Figure 1.** Presenting the charging curves of $Li_5FeO_4$, $Li_{5.5}Fe_{0.5}Co_{0.5}O_4$, and $Li_6CoO_4$ in a loop. The figure shows two characteristic changes, with two distinct voltage plateaus labeled as Stage I and Stage II [20].

Such reactions not only consume active $Li^+$, but also form insulating LiOH and $Li_2CO_3$ passivation layers on the LFO surface, which block $Li^+$ diffusion and increase interfacial impedance. The experimental results show that after LFO is exposed to air for 24 h, the proportion of $Li_2CO_3$ on its surface can reach 62%, and the initial delithiation capacity attenuation exceeds 75%. Additionally, these alkaline by-products dissolved in NMP, the commonly used solvent for cathode slurry, will induce slurry gelation and seriously damage the processing performance [17]. This failure mode has promoted the development of surface doping modification strategies, which aim to reduce the adsorption affinity of $H_2O/CO_2$ and suppress interfacial side reactions by regulating the surface electronic structure of LFO.

### 2.3.2 Migration and lattice collapse during the delithiation process

The structural transformation from the antifluorite phase to the disordered rock-salt phase during delithiation exhibits kinetic irreversibility, which originates from the asymmetry of the $Fe^{3+}$ migration energy barrier: the forward migration energy barrier of $Fe^{3+}$ from the tetrahedral site to the octahedral site is only 0.25 eV, while the reverse barrier is as high as 0.9 eV [16]. This asymmetry "locks" $Fe^{3+}$ in the octahedral sites after delithiation, making it impossible to reversibly restore the antifluorite phase and resulting in permanent structural degradation. In addition, the extraction of 4 mol $Li^+$ per LFO molecule will induce a volume contraction of approximately 18%, generating huge lattice strain that causes micron-sized single-crystal LFO particles to fracture into polycrystalline nanoparticles. The newly exposed fresh surfaces further accelerate interfacial side reactions and oxygen release, forming a positive feedback loop of capacity degradation [15,18]. The post-cycling characterization of LFO-containing all-solid-state batteries reveals that a large number of cracks appear in the particles after 100 cycles, which directly confirms the correlation between Fe migration-driven lattice collapse and mechanical failure [18]. Doping modification targeting Fe-site pinning or lattice strain relaxation is the core approach to mitigate this type of failure [18].

### 2.3.3 The gas evolution origin of $O_2$ precipitation

The origin of $O_2$ release during the deep delithiation process lies in the unique electronic structure of LFO. DFT calculations identify

a type of "Li-only coordinated" O atoms in LFO (referred to as the $A_6$-O configuration), which are only coordinated by surrounding $Li^+$ without adjacent Fe cations. Its O 2p orbital has a high density of states contribution near the Fermi level, serving as the main active site for anionic redox [15,25]. During deep delithiation, electrons are preferentially lost from these O 2p orbitals to form $O^-$ radicals, which rapidly dimerize and desorb from the lattice into $O_2$ molecules. $O_2$ precipitation will not only oxidize liquid/sulfide solid electrolytes to generate high-impedance interfacial by-products and gas bulging, but also induce the formation of oxygen vacancies, further undermining the lattice stability [15,18,21]. Enhancing the covalent bonding between O and adjacent cations via doping, or introducing redox-inert cations to dilute the $A_6$-O configuration, are the key doping directions for suppressing $O_2$ release and improving safety.

The above three types of failure mechanisms directly guide the design principles of LFO doping modification: (1) Surface active doping to inhibit $H_2O/CO_2$ adsorption; (2) Lattice site doping to pin $Fe^{3+}$ and reduce lattice strain; (3) Electronic structure regulation to stabilize anionic redox and suppress $O_2$ precipitation.

It should be stressed that the three types of mechanisms rarely run independently, and they exhibit intense mutual coupling during actual delithiation reactions. In the first voltage plateau, the migration of $Fe^{3+}$ not only transforms the crystal structure into a disordered rock-salt phase but also result in the fracture of micron-sized particles. This process continuously generates newly exposed surfaces, which are full of undercoordinated $Li^+$ sites. Compared with the original material surface, these new surfaces have stronger adsorption capacity for $H_2O$ and $CO_2$, accelerating harmful interfacial side reactions and forms thick insulating passivation layers. Meanwhile, deep delithiation at the high-voltage plateau induces oxygen release from the $A_6$-O structural unit. The released oxygen further oxidizes the electrolyte and produces acidic substances (e.g., HF), which in turn attacks the LFO surface and aggravate lithium ions dissolution. This positive feedback loop makes the degree of capacity degradation far exceed the sum of individual mechanisms. The coupled degradation processes reveal the root cause of performance deterioration and deliver definite theoretical guidance for the doped modification of LFO. Practical doping schemes need to coordinately restrain multiple degradation routes at the same time. For instance, $Zr^{4+}$ doping pins $Fe^{3+}$ within tetrahedral lattice positions to prevent particle cracking caused by cation migration, while $F^-$ substitution stabilizes lattice anionic redox behavior and suppresses oxygen evolution side reactions, and $Na^+$ occupying lithium lattice sites reduces the chemical activity of surface lithium and inhibits the adsorption of water and carbon dioxide. Only by jointly restraining these interconnected degradation paths can LFO meet practical application requirements.

Combined with the above analysis of failure mechanisms and corresponding doping design ideas, the following part of this chapter systematically summarizes various elemental doping strategies and elaborates on how these methods improve the electrochemical properties of LFO.

## 3. Progress in element doping modification of $Li_5FeO_4$

Aiming at the problems exposed in the cathode prelithiation application of LFO, such as poor air stability, low electrical conductivity, unstable solid-liquid interface of the battery, and incomplete delithiation at high rates, researchers mainly optimize the materials from two directions: surface coating and bulk doping [26,27]. Surface coating (such as carbon layer and oxide layer) suppresses the erosion of air and electrolyte through physical isolation, effectively reduces surface residual alkali and slows down the erosion of active oxygen to the electrolyte, thus significantly improving the interfacial stability of the material [28,29]. Bulk doping regulates the lattice structure by introducing heterogeneous ions, reduces the $Li^+$ migration energy barrier and narrows the band gap, thereby promoting phase transition kinetics and charge transfer, and improving the delithiation capacity at high rates [20,30]. In this chapter, we comprehensively summarize the current research on the doping modification of LFO, and discuss the effects of doping on the crystal structure, phase transition behavior, and electrochemical performance, so as to contribute to exploring a wider range of doping modification strategies for LFO.

### 3.1 Fe-site cation doping

Among various doping strategies, Fe-site cation substitution represents the most intensively investigated approach, as it directly modes the redox-active center responsible for charge compensation during delithiation. By partially replacing $Fe^{3+}$ with aliovalent or isovalent cations, researchers aim to tailor the electronic structure, suppress Fe migration, and mitigate lattice oxygen release. The following section summarizes representative Fe-site dopants and their respective regulatory effects.

To investigate the effect of Co doping content on the structure and electrochemical performance of $Li_{5+x}Fe_{1-x}Co_xO_4$, a series of samples with Co doping ratios of 0, 5%, 10%, 12.5%, and 25% have been synthesized, respectively. Structural analysis shows that with the increase of Co content, the crystal structure gradually transforms from the α phase ($Fe^{3+}$ occupies three $Li^+$ sites) to the β phase ($Co^{2+}$ occupies two $Li^+$ sites) [31]. Electrochemical tests show that the first charge curve of the α phase presents two voltage plateaus at approximately 3.5 V and 4.0 V, while the β-phase $LF_6C_2O$ ($Li_{5.25}Fe_{0.75}Co_{0.25}O_4$) exhibits three plateaus at about 3.3 V, 3.9 V, and 4.2 V, thus delivering a higher irreversible specific capacity. It is worth noting that after the α-phase structure is exposed to air (relative humidity of 60%) for 0.5 h, its 3.5 V plateau almost disappears, and the prelithiation capacity degrades significantly. In contrast, $LF_6C_2O$ still maintains a specific capacity above 700 $mAh \cdot g^{-1}$, which confirms that the β phase has superior air stability. X-ray photoelectron spectroscopy (XPS) and scanning electron microscopy (SEM) test results further show that a rough surface reaction layer is rapidly formed on the LFO after exposure to air. This is because the generation of $Li_2CO_3$ and water adsorption. However, the $LF_6C_2O$ only has slight changes and keeps a smooth morphology, which demonstrates its better surface stability. According to the transition metal dissolution test results, the dissolution of Fe and Co are significantly reduced when the Co content increases to 25%. It highlights the key maintaining effect of the crystal structure on the stability of the M–O framework. $LF_6C_2O$ prelithiated battery delivers an initial charge capacity of 234 $mAh \cdot g^{-1}$ at 0.05 C, outperforming LFO battery in practical battery applications. It also exhibits a better capacity retention after 100 cycles at 1 C, accompanied by a lower oxygen evolution amount. Considering comprehensively factors including air stability,

electrochemical performance, and cost, 25% Co doping is determined as the optimal ratio. It is reported a study on introducing Co at the Fe site to enhance the lithium compensation effect [32]. Its mechanism proposes that Co doping promotes the stepwise oxidation transformation of $O^{2-} \rightarrow O_2^{n-} \rightarrow O_2$, which induces local structural distortion, thereby prompting more lattice oxygen in $Li_{5.5}Fe_{0.5}Co_{0.5}O_4$ (LFCO) to participate in the charge compensation process. In addition, the air stability of LFCO is significantly enhanced: after being exposed to air for 4 days, its initial capacity still remains at 520.8 mAh·g$^{-1}$, while LFO exhibits obvious capacity degradation. When LFCO is used as a prelithiation additive in graphite||NCM811 full cells, a specific capacity of 210.5 mAh·g$^{-1}$ can be obtained at 0.1 C rate, and the capacity retention rate is as high as 89.6% after 200 cycles.

Furthermore, a defect engineering strategy, which introduces $Zr^{4+}$ at the tetrahedral Fe site to promote the formation of $Li^+$ vacancies and reduce the migration energy barrier, is employed to significantly enhance the Li+ diffusion kinetics and lithium compensation capacity, enabling LFO–$Zr_{0.03}$ to exhibit high capacity and excellent rate performance (Figure 2(a-c)) [33]. The galvanostatic intermittent titration technique (GITT) test shows that the second delithiation plateau of LFO–$Zr_{0.03}$ is significantly prolonged (Figure 2(d)), and its $Li^+$ diffusion coefficient ($10^{-12.5}$ cm$^2$·s$^{-1}$ to $10^{-9.5}$ cm$^2$·s$^{-1}$) is much higher than that of LFO (Figure 2(e)), which is attributed to the lithium vacancies and reduced energy barrier induced by Zr doping. Meanwhile, electrochemical impedance spectroscopy (EIS) results confirm that the interfacial impedance of this material is lower than that of LFO both in the initial state and after cycles, which further corroborates its fast kinetic characteristics and interfacial stability. Compared with other prelithiation materials, LFO–$Zr_{0.03}$ exhibits significant advantages in multiple performance indicators (Figure 2(f)).

The manganese doping strategy have shown that compared with LFO, prelithiation with LFMO ($Li_{5.125}Fe_{0.875}Mn_{0.125}O_4$) can effectively improve the interfacial composition of lithium iron phosphate (LFP) batteries [34]. EIS shows that the SEI impedance ($R_{SEI}$) of the prelithiated battery after cycles is lower than that of the nonprelithiated battery. Further XPS analysis shows that LFMO prelithiation promotes the generation of LiF component in the SEI film, while reducing the content of $Li_2CO_3$. Although the introduction of Mn accelerates the decomposition of $LiPF_6$ and FEC in the electrolyte and thickens the interfacial layer to a certain extent, it optimizes the composition of the SEI layer, reduces the interfacial impedance, and forms a more stable and dense interfacial structure on the whole, thus significantly improving the cycling stability of the battery.

## 3.2 Non-Fe-site ion doping

In addition to Fe-site modification, Li-site and O-site doping provide alternative tactics to optimize LFO performance. Fe-site doping mainly alter redox centers, while non-Fe-site doping expands lithium diffusion paths and stabilizes the crystal skeleton. This section reviews recent developments in Li-site cation doping, O-site anion doping and emerging Co-doping approaches. In addition to the above-mentioned $Fe^{3+}$ site doping strategies, Zhu *et al.* [35] also explored the Li-site doping strategy, proposing to introduce $Na^+$ at the Li site of the tetrahedral framework to synthesize LFO–Na material for enhancing the lithium compensation capacity. Characterizations including energy dispersive spectrometer (EDS), focused ion beam-scanning electron microscopy (FIB-SEM) etching, and XPS confirm that $Na^+$ is successfully introduced into the bulk phase. Electrochemical tests show that the initial charge capacities of LFO–$Na_{0.02}$ at 0.1 C and 1 C rates reach 763.8 mAh·g$^{-1}$ and 584.2 mAh·g$^{-1}$ respectively, which are 86.2 mAh·g$^{-1}$ and 221.7 mAh·g$^{-1}$ higher than those of LFO. In addition, LFO–Na still maintains a capacity of 531.0 mAh·g$^{-1}$ after being exposed to air with 20% relative humidity for 8 h, while the pristine LFO only retains 249.2 mAh·g$^{-1}$, demonstrating excellent air stability. The reaction mechanism of LFO–Na can be summarized as follow: the introduction of $Na^+$ effectively reduces the migration energy barrier of $Li^+$, promotes lattice oxygen to participate in redox reactions, and drives oxygen species to gradually transform from the initial $O^{2-}$ to $O_2$ via the intermediate state $O_2^{n-}$, thus significantly enhancing the lithium compensation capacity of LFO.

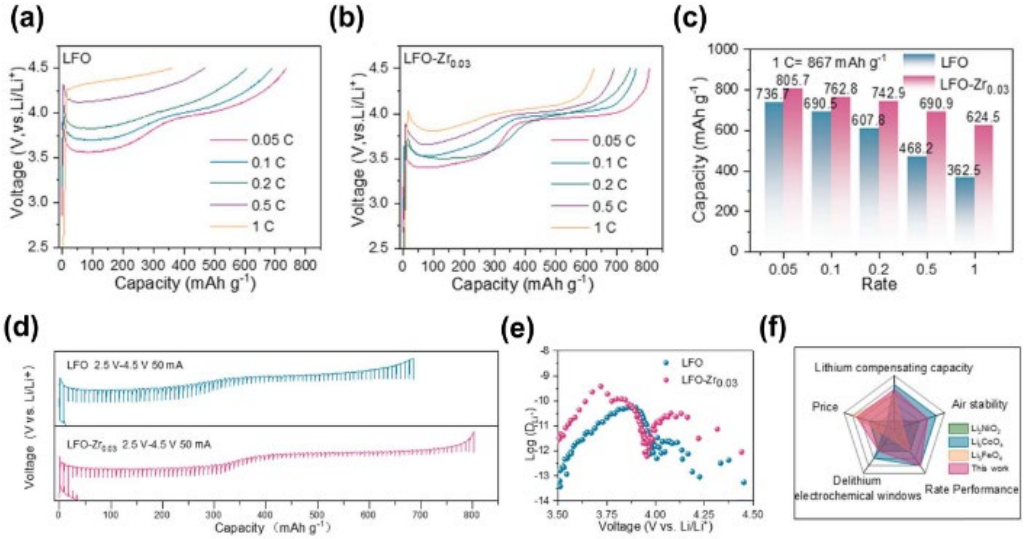


**Figure 2.** Electrochemical performance of LFO and LFO–$Zr_{0.03}$ electrodes at 25°C within 2.5 V to 4.5 V. (a, b) Initial charge curves; (c) initial charge capacity at various rates; (d) GITT profiles and (e) the corresponding log ($D_{Li^+}$)-potential plots during charge; (f) this radar chart sets five evaluation indicators, to intuitively compare the comprehensive advantages and disadvantages of LFO-$Zr_{0.03}$ and other pre-lithiation materials [33].

Although both Li-site and O-site doping enhance LFO properties, the underlying optimization principles of the two methods differ drastically. When $Na^+$ serves as the dopant, it mainly occupies Li lattice sites, therefore expanding the migration tunnels for $Li^+$ and triggering lattice oxygen activity. $F^-$ doping replaces oxygen sites to strengthen chemical bonds. Its core advantage lies in restraining oxygen escape and enhancing the material's resistance against humid air. Overall, the selection of modification strategies is determined by actual application goals.

Different from the cation doping strategies, an anion doping route has been pioneered, using polyvinylidene fluoride (PVDF) pyrolysis to fluorinate the air-stable lithium ferrite prelithiation material, realizing surface fluorine doping and bulk gradient fluorination, and revealing the effect of fluorination on the crystal structure of LFO for the first time [36]. Studies have found that the substitution of $F^-$ for $O^{2-}$ leads to an increase in unit cell parameters, which originates from the fact that part of $Fe^{3+}$ is reduced to $Fe^{2+}$ with a larger ionic radius to maintain charge balance. Combined with in-situ X-ray diffraction (XRD), electrochemical impedance spectroscopy (EIS), differential electrochemical mass spectrometry (DEMS), and theoretical calculations, this study further demonstrates that the high energy barrier of iron migration leads to sluggish phase transition kinetics, which is the intrinsic reason for the unsatisfactory initial charge specific capacity of LFO at high state of charge. Fluorine doping effectively expands the tetrahedral gap at the iron center, promotes the migration of iron during the phase transition process, narrows the band gap at the same time, and accelerates charge transfer. The thus-obtained LFOF@FC-7 material exhibits excellent air stability (maintaining 541.9 $mAh \cdot g^{-1}$ after 24 h of exposure to humid air) and maintains stable phase transition at high current density. Its initial charge specific capacity at 1.0 C rate reaches 580.5 $mAh \cdot g^{-1}$, which is much higher than the 325.1 $mAh \cdot g^{-1}$ of pristine LFO. In addition, fluorination also reduces the erosion of the electrolyte by active oxygen during the charging process, generating only a tiny amount of $CO_2$. Although the above studies demonstrate the potential of doping modification in improving the prelithiation performance of LFO, overall, the research on LFO doping systems is still in its infancy. A systematic understanding of the screening and synergistic effects of different doping elements has not yet been formed, and the regulation law of doping on the structural evolution and charge compensation mechanism during the prelithiation process also remains to be further explored.

## 4. First-principles studies on doped $Li_5FeO_4$

First-principles studies are widely employed to unravel the atomic-scale mechanisms of prelithiation and the role of dopants. By examining lattice relaxation, the density of states, and ion-migration barriers, these analyses link macroscopic electrochemical behavior to the local atomic environment [37,38]. In particular, first-principles calculations offer essential insights into doping mechanisms and the resulting structure–property relationships. These insights guide the rational design of doping strategies, thereby accelerating the development and application of doped LFO prelithiation additives in high-performance lithium-ion batteries [39,40]. Table 1 summarizes the main computational parameters employed in recent DFT studies on the LFO system, in which " — " denotes that the parameter was not reported in the cited work. The Vienna Ab initio Simulation Package (VASP) provides DFT calculation scheme for the studied system. Numerical configurations consist of the projector augmented wave (PAW) approach, a plane-wave energy cutoff of 520 eV, and the Perdew–Burke–Ernzerhof (PBE) functional, which is based on generalized gradient approximation (GGA). In addition, spin polarization treatment and Hubbard U on-site correction are introduced for electronic structure calculations.

It is inevitable that calculated parameters, like bandgap and formation energy, show numerical deviations when researchers select different Hubbard U values. Nevertheless, doping trigger performance variations maintain the same overall trend in qualitative analysis. For example, Augustine *et al.* employed U = 4.0 eV for Fe and proved that Ti substitution decreases the bandgap from 2.78 eV to approximately 1.0 eV [41]. In contrast, Wang *et al.* used U = 5.3 eV and observed Co doping optimizes the thermodynamic stability by lowering the formation energy of the β phase against the α phase [31]. These two studies both support that heterovalent cation doping improves electrical conduction and structural stability. Two separate CI–NEB investigations further illustrate this rule. In the studies, Zhu et al. selected U = 5.3 eV and Wang *et al.* chose U = 4.0 eV, they both pointed out that transition metal doping reduces $Li^+$ hopping barriers by 0.1 eV to 0.15 eV [33,34]. The root of this unified trend can be attributed to the orbital overlap and local lattice distortion dominated doping effects. Different from the absolute energy values of electronic states, these physical factors barely respond to U adjustments. Accordingly, core viewpoints summarized in this paper will not be undermined by different U selections.

**Table 1.** Summary of the main DFT calculation settings for the LFO system.

| Dopants | Pseudopotential/ Functional | +U [eV] | Spin treatment | k-point sampling | Convergence criteria | | Gaus-sian smea-ring | Ref. |
|---|---|---|---|---|---|---|---|---|
| | | | | | Force | Energy | | |
| Co | PAW/GGA-PBE | Fe : 5.3; Co : 3.32 | — | MP grid : 4×4×4 (relax.); 6×6×6 (DOS) | 0.02 $eV \cdot Å^{-1}$ | $10^{-4}$ eV | — | [31] |
| Co | —/GGA | Fe : 4.0 | Yes | MP spacing : 0.03 $Å^{-1}$ (relax.) | 0.02 $eV \cdot Å^{-1}$ | — | 0.01 eV | [32] |
| Zr | PAW/GGA-PBE | Fe : 5.3 | Yes | ≥1200 k-points per reciprocal atom | 0.03 $eV \cdot Å^{-1}$ | $10^{-5}$ eV | 0.05 eV | [33] |
| Mn | PAW/GGA-PBE | Fe : 4.0; Mn : 3.9 | — | MP grid : 4×4×4 (relax.); 6×6×6 (DOS) | 0.02 $eV \cdot Å^{-1}$ | $10^{-4}$ eV | — | [34] |
| Na | —/GGA | Fe : 4.0 | Yes | MP spacing : 0.03 $Å^{-1}$ (relax.) | 0.02 $eV \cdot Å^{-1}$ | — | 0.01 eV | [35] |
| F | —/GGA | Fe : 4.0 | Yes | MP spacing : 0.03 $Å^{-1}$ (relax.) | 0.02 $eV \cdot Å^{-1}$ | — | 0.01 eV | [36] |
| \ | PAW/GGA-PBE | Fe : 4.0 | — | Γ-centered; 8000 k-points per reciprocal atom | — | — | — | [19] |
| Ti | PAW/GGA | Fe : 4.0; Ti : 3.6 | Yes | MP grid: 4×4×4 (relax.); 6×6×6 (DOS) | — | $10^{-6}$ $eV \cdot atom^{-1}$ | — | [41] |

### 4.1 Density of states calculations

The density of states (DOS) presents the distribution of electronic energy levels and electronic structure within material. DOS is usually divided into total DOS (TDOS) and partial DOS (PDOS) [42]. TDOS can help scientists judge the band gap. From this, we can learn how doping modifies electronic conductivity. PDOS further breaks down the TDOS into contributions from individual atomic orbital, revealing the atomic-scale origins of redox activity in LFO [43].

A large number of LFO studies mainly centered on electrochemical properties. But the oxygen redox behavior remains poorly understood. Zhan *et al.* [19] were the first to uncover the coupled Fe–O redox mechanism together with dynamic structural variation of LFO by integrating systematic experimental tests and first-principles calculations. They examined DOS, charge density and spin density near oxygen sites. These analyses revealed how the local configuration governs oxygen redox activity. DFT calculations indicated that the $O^-$ ions reside in a "$Li_6$–O" configuration in the $Li_3FeO_{3.5}$ phase, in which oxygen is coordinated only by Li, whereas every $O^{2-}$ connects to one or more Fe atoms. Comparative analysis on PDOS values shows that the intensity of oxygen states in the $Li_6$–O configuration is greatly higher than that of Fe states. The prominent oxygen contribution can be attributed to the concentrated electron clouds around oxygen ions confirmed by charge density calculations, and these electronic states match the energy position for single-electron extraction. Totally, these results validate the oxidation reaction $O^- \rightarrow O^0$ occurring inside the $Li_6$–O configuration.

Anu Maria Augustine's team [41]carried out TDOS and PDOS calculations on $Li_5Fe_{1-x}Ti_xO_4$ at multiple Ti substitution fractions. Their outputs show that undoped $Li_5FeO_4$ is a wide-bandgap insulator of 2.78 eV with both the VBM and CBM dominated by hybridized Fe-d and O-p orbitals. Partial Ti incorporation introduces localized $Ti^{3+}$ d states inside the bandgap. The effective bandgap drops to approximately 1.0 eV, and the enhanced electronic conductivity is observed. In contrast, when Fe is fully replaced by Ti (x = 1.0), the bandgap expands to 1.65 eV instead, owing to the loss of the Fe-d contribution at the CBM. These observations demonstrate that the partial Ti substitution is more favorable for the conductivity improvement. The DOS investigation describes band structure variation caused by doping, meanwhile, it locates where in gap states originate at atomic level as well, providing promising strategy to build rational gradient doping.

### 4.2 Formation energy calculations

Generally, thermodynamic stability is assessed by formation energy. A more negative formation energy means that the material is the more stable. For example, the formation energy of Mn-doped LFO was calculated based on Equation (4) [34]:

$$\Delta E_f^{Li_{5+x}Fe_{1-x}Mn_xO_4} = \frac{E_{Li_{5+x}Fe_{1-x}Mn_xO_4} - (\Sigma N_M \times \mu_M^{bulk})}{\Sigma N_M} \quad (4)$$

where E corresponds to the total energy for geometry optimization $Li_5Fe_{1-x}Mn_xO_4$ unit cell. $N_M$ and μ represent the number of corresponding elements within the unit cell and single-atom energy from singlet-point energy computations, respectively. Comparison among different Mn doping ratios, it is found that higher Mn content yields more negative formation energies, indicating the enhanced thermodynamic stability. Except for doping concentration, formation energy can identify preferred doping site as well. Wen *et al.* [36] computed the formation energy for F substituting different O sites. $O_3$ site produces the minimum energy, indicating the preferential site for F substitution.

Moreover, the formation energy can be used to determine the phase transitions and structural stability. Wang *et al.* [31] constructed α phase ($Fe^{3+}$ occupying three Li sites) and the β phase ($Co^{2+}$ occupying two Li sites) at various Co doping levels. The obtained results revealed that the β phase shows a lower formation energy than α phase at 50% Co doping, which is indicated for a structural transformation. This matches experimental results that $Li_{5.125}Fe_{0.875}Co_{0.125}O_4$ spontaneously changes structure after only 0.5 h of air exposure. All in all, formation energy is a flexible thermodynamic criterion. It is useful for doping sites screening, doping concentrations optimization and phase stability evaluation, so that it becomes an important theoretical tool to understand the thermodynamic mechanisms of doping modification.

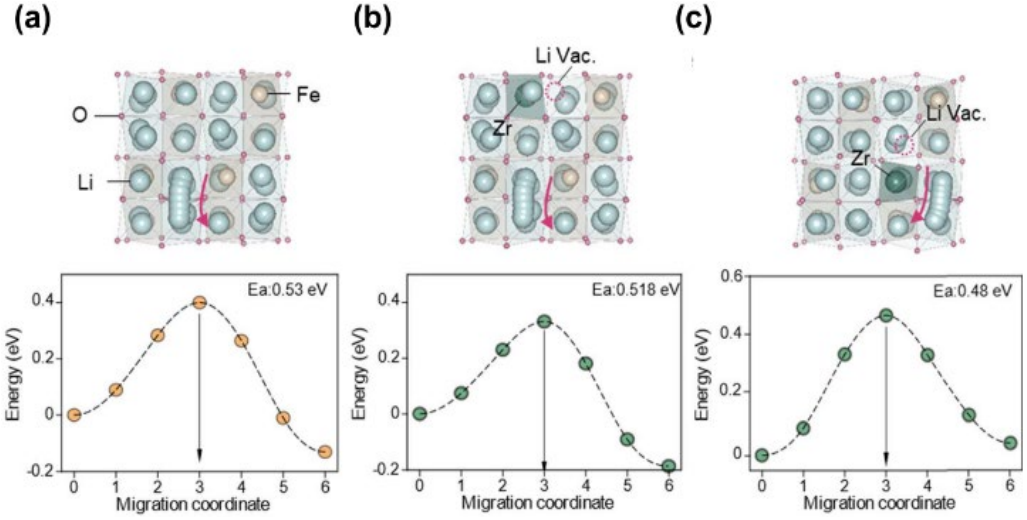


**Figure 3.** $Li^+$ migration pathways and energy barriers calculated by CI–NEB: (a) pristine $Li_5FeO_4$, (b, c) Zr-doped $Li_5FeO_4$. Atoms like Li, Fe, Zr and O are colored respectively blue, yellow, green and pink. Li vacancies are marked pink dashed circles and red arrows label migration paths [33].

### 4.3 Climbing image nudged elastic band calculations

To gain deeper insight into the effect of doping on $Li^+$ diffusion behavior, the climbing image nudged elastic band (CI–NEB) method is frequently employed to simulate the migration pathways and energy barriers of $Li^+$ in the LFO system [44]. Dopants can alter the local coordination environment and diffusion channels of $Li^+$, thereby optimizing the delithiation pathway [45]. Fast and efficient compensation of active lithium during the initial charge of prelithiation additives relies on superior ionic diffusion kinetics [46].

Zhu *et al.* [33] studied the effect of Zr doping on the high-rate delithiation of LFO–Zr by comparing the Li migration pathways in pristine LFO and Zr-doped LFO. In pristine LFO, Li migration from one tetrahedral site to a neighboring tetrahedral site proceeds via a distorted tetrahedral transition state with a barrier of 0.53 eV (Figure 3(a)). For LFO–Zr, two distinct tetrahedron-to-tetrahedron diffusion paths were examined: one in which the initial tetrahedron shares an edge with an $FeO_4$ unit (Figure 3(b)), and another in which it shares an edge with a $ZrO_4$ unit (Figure 3(c)). These paths yield lower barriers of 0.518 eV and 0.48 eV, respectively. Moreover, $Li^+$ diffusion is strongly concentration-dependent; Li vacancies introduced by Zr doping can further facilitate $Li^+$ migration.

Similarly, Wang *et al.* [34] similarly used CI–NEB calculations to assess the effect of Mn substitution on $Li^+$ diffusion in LFO, focusing on the migration pathway around the Fe/Mn–O tetrahedra. The barrier profiles obtained from calculation give 0.51 eV as the maximum diffusion barrier for pristine LFO, consistent with Zhu *et al.*'s data of 0.53 eV. For Mn-doped $Li_{5.125}Fe_{0.875}Mn_{0.125}O_4$ (LFMO) and $Li_{5.5}Fe_{0.5}Mn_{0.5}O_4$ (LFMO-1), the maximum barriers drop to 0.39 eV and 0.37 eV. Mn substitution raises $Li^+$ content and decreases transition-metal valence states. More active lithium becomes available, so capacity and electrochemical performance get improved. Moreover, Mn-doped systems hold more stable final-state energies, as the consequence of the difference of local $Li^+$ surroundings between start and end sites. It provides extra evidence that doping adjusts thermodynamic stability for diffusion pathways. Zr doping and Mn substitution lower the $Li^+$ migration barriers by altering the local structure of the transition-metal-oxygen tetrahedra and modifying the Li vacancy numbers. These results demonstrate CI–NEB calculations can guide the design of LFO for fast $Li^+$ diffusion kinetics.

### 4.4 Ab Initio molecular dynamics simulations

Li *et al.* [47] further employed ab initio molecular dynamics (AIMD) simulations to explore the possible formation of O–O dimers in $Li_5FeO_4$. The simulations revealed that in the $Li_3FeO_{3.5}$ phase, oxygen atoms belonging to the $Li_6$–O units form O–O dimers with bond lengths below 1.6 Å within 15 ps at both room temperature (300 K) and 1000 K. These dimers originate exclusively from the $Li_6$–O units and their appearance coincides with the disappearance of these units. As the simulation proceeds, the O–O bond length shortens from 1.55 Å to 1.43 Å, values that match the characteristic bond lengths of peroxide ($O_2^{2-}$) in $Li_2O_2$ and superoxide ($O_2^-$) in $LiO_2$, respectively. This suggests that both peroxide and superoxide species form in $Li_3FeO_{3.5}$. First-principles calculations have provided crucial insight into the intrinsic redox activity of LFO and the mechanisms of doping modification. However, theoretical efforts to date have largely focused on the electronic structure and ion migration in doped systems, while systematic assessments of air stability and solid-liquid interfacial stability under practical operating conditions remain scarce. The commercial prospect of LFO prelithiation additives is mainly affected by its stability under processing conditions and the compatibility with interfaces of battery. Thus, additional theoretical works in these directions are urgently needed.

## 5. Conclusions and outlook

LFO is considered as a promising cathode prelithiation additive owing to its combination of high theoretical delithiation capacity, stable delithiated products, suitable delithiation potential as well as low cost. However, several obstacles hinder its commercial application, such as incomplete delithiation, poor air stability, and low electronic conductivity. To overcome these challenges, the surface coating and bulk doping strategies have been widely carried out. Surface coatings act as physical barriers that protect the material from air and electrolyte attack, thereby largely improving the interfacial stability. Bulk doping, on the other hand, incorporates heteroatoms, which tune the local lattice structure, lower the Li migration barrier, and narrow the bandgap to enhance electronic conductivity. These modifications facilitate phase-transition kinetics and charge transfer, leading to the improved high-rate delithiation capacity.

This review surveys recent advances in the doping modification of LFO and the corresponding application of first-principles calculations. Studies on Fe-site cation doping and non-Fe-site ion doping have presented valuable insights. Using first-principles descriptors such as formation energy, density of states, and migration barriers, researchers have clarified the atomic-scale origins of LFO's redox activity and the ways in which dopants enhance material properties. These findings offer a basis for the rational design of more effective doping strategies. Despite the commercial promise of LFO, several challenges for prelithiation technology still need to be addressed below.

The synergistic effects of various doping strategies are still poorly understood. Up to now, most studies have focused on single-element doping at a single site, whereas multi-element co-doping remains largely unexplored. Key issues such as the competitive site occupancy of different dopants, the underlying charge compensation mechanisms, and their coupled impact on Fe/O redox activity have yet to be clarified. Meanwhile, high-throughput DFT calculations combined with machine-learning could facilitate to establish multi-dimensional descriptors for rapidly screening promising dopant combinations, thereby building a candidate library to guide experimental synthesis and accelerate the discovery of high-performance materials.

The scope of theoretical calculations needs to be broadened. First-principles studies on LFO have so far focused largely on the electronic structure and ion migration of doped systems, while systematic assessments of air stability and solid–liquid interfacial stability under realistic conditions remain scarce. Future works are suggested to pay attention on interfacial simulations, quantifying and the mechanisms involving the dopants modulate interfacial reaction barriers at the atomic scale, which would provide predictive guidance for enhancing the processing tolerance and operational stability of LFO.

In summary, research on LFO prelithiation additives is now moving from fundamental understanding toward performance-driven design.

By combining doping design, interface engineering, in-situ characterization, and AI-assisted screening, further breakthroughs in doping strategies, material synthesis, and reaction mechanisms are expected, which will accelerate the large-scale development of prelithiation technology and provide a viable route for next-generation high-energy-density lithium-ion batteries.

## Acknowledgements

This work was supported by Youth Teacher Research and Cultivation Fund of South China Normal University (Project No. 671866), presided over, 30000 yuan and Natural Science Foundation of Shanghai (25ZR1402156).

## References

[1] P. Kantichaimongkol, T. Wanotayan, and J. Qin, "Review on surface engineering of NMC for high performance of lithium-ion batteries," *Journal of Metals, Materials and Minerals*, vol. 35, no. 2, p. e2338, 2025.

[2] S. Sahu, and N. Devi, "Lactic acid-assisted complexation for enhanced lithium extraction and its application to spent LIBs," *Journal of Metals, Materials and Minerals*, vol. 35, no. 1, p. e2245, 2025.

[3] L. Zhuang, W. Cai, H. Ji, Q. Li, G. Wang, S. Xin, Q. Zhao, F. Cheng, Y. Guo, L. Mao, Y. Tian, F. Wu, L. Zhang, Y. Xiang, J. Hu, R. Cao, L. Xiao, H. Tao, W. Xing, D. Zhan, H. Liao, M. Xiao, B. Ren, Z. Peng, R. Wen, X. Wang, Y. Song, H. Lv, B. Xia, G. Wang, J. Cheng, Z. Liu, M. Zhou, B. Huang, C. Li, Y. Zou, S. Wang, H. Lin, and Z. Wei, "Development Trends and Priority Research Fields of Electrochemical Discipline in the 15th Five Year Plan Period," *Journal of Electrochemistry*, vol. 31, no. 10, p. 2510081, 2025.

[4] B. Li, K. Zhang, B. Yu, R. Yan, X. Jiang, S. Zhang, B. Yang, and Y. Yao, "Achieving cycling stability of silicon-based anodes for lithium-ion batteries: From lithium storage/failure mechanism to structure optimization," *Journal of Energy Storage*, vol. 136, p. 118395, 2025.

[5] K. Qin, T. Xu, C. Tian, C. Tan, H. Yu, and L. Suo, "Correlating volume expansion and cycle life in anode-free lithium-metal pouch cells," eScience Energy, vol. 24, p. 100076, 2026.

[6] C. Xu, Z. Wang, S. Li, J. Jiang, and Z. Ju, "Research progress and engineering application prospects of prelithiation technology for lithium-ion batteries," *Energy Storage Science and Technology*, vol. 14, no. 3, pp. 930–946, 2025.

[7] W. Zhong, Z. Zeng, S. Cheng, and J. Xie, "Advancements in prelithiation technology: Transforming batteries from Li-shortage to Li-Rich systems," *Advanced Functional Materials*, vol. 34, no. 2, p. 2307860, 2024.

[8] F. Zhao, S. Chen, C. Song, Y. Jiang, K. Yang, Y. He, and X. Liu, "Photo-enhanced reaction engineering for advanced lithium-sulfur batteries: From mechanisms and materials to system design," *eScience Energy*, vol. 5, p. 100026, 2026.

[9] C. Tan, Z. Che Daud, Z. Asus, M. Idris, I. Mazali, M. Ardani, and M. Abdul Hamid, "A holistic review on the synthesis techniques of spinel structured lithium cobalt manganese tetroxide," *Journal of Metals, Materials and Minerals*, vol. 32, no. 4, pp. 59–70, 2022.

[10] M. Sun, K. Tang, and Z. Xu, "Addressing lithium deficiency in anode-free lithium metal batteries: Design principles and supplementation strategies," *Small Science*, vol. 5, no. 10, p. 2500254, 2025.

[11] S. Li , J. Jiang, Y. Zheng, Z. Ju, Q. Zhuang, K. Wu, H. Shao, and X. Zhang, "Pre-lithiation technology for rechargeable lithium-ion batteries: Principles, applications, and perspectives," *Batteries & Supercaps*, vol. 7, no. 7, p. e202400115, 2024.

[12] K. Park, B.-C. Yu, and J. B. Goodenough, "$Li_3N$ as a cathode additive for high-energy-density lithium-ion batteries," *Advanced Energy Materials*, vol. 6, no. 10, p. 1502534, 2016.

[13] X. Liu, T. Liu, R. Wang, Z. Cai, W. Wang, Y. Yuan, R. Shahbazian-Yassar, X. Li, S. Wang, E. Hu, X. Yang, Y. Xiao, K. Amine, J. Lu, and Y. Sun, "Prelithiated Li-enriched gradient interphase toward practical high-energy NMC–silicon full cell," *ACS Energy Letters*, vol. 6, no. 2, pp. 320–328, 2020.

[14] W. Wang, X. Jia, Y. Zhang, B. Qin, Y. Wang, C. Yang, and Q. Liu, "Rational process design of cost-benefit prelithiation additive $Li_5FeO_4$ enables high-performance lithium-ion batteries," *Journal of Power Sources*, vol. 674, no. 239774, pp. 239774.1–239774.7, 2026.

[15] C. S. Johnson, S.-H. Kang, J. T. Vaughey, S. V. Pol, M. Balasubramanian, and M. M. Thackeray, "$Li_2O$ Removal from $Li_5FeO_4$: A cathode precursor for lithium-ion batteries," *Chemistry of Materials,* vol. 22, no. 3, pp. 1263–1270, 2010.

[16] Z. Yao, M. K. Y. Chan, and C. Wolverton, "Exploring the origin of anionic redox activity in super Li-rich iron oxide-based high-energy-density cathode materials," *Chemistry of Materials*, vol. 34, no. 10, pp. 4536–4547, 2022.

[17] B. Zhu, W. Zhang, Q. Wang, Y. Lai, J. Zheng, N. Wen, and Z. Zhang, "Understanding the air-exposure degradation chemistry of the sacrificial cathode additive $Li_5FeO_4$ for Li-ion batteries," *Advanced Functional Materials*, vol. 34, no. 22, p. 2315010, 2024.

[18] X. Xu, S. Chu, S. Xu, H. Li, C. Sheng, M. Dong, S. Guo, and H. Zhou, "Integrating prelithiation and interface protection to achieve high-energy all-solid-state batteries," *Angewandte Chemie International Edition*, vol. 64, no. 4, p. e202415891, 2025.

[19] C. Zhan, Z. Yao, J. Lu, L. Ma, M. Victor A, L. Li, L. Eungje, A. Esen E, T. Wu, J. Wen, Y. Ren, J. Christopher, T. Michael M, C. Maria K. Y., W. Chris, and A. Khalil, "Enabling the high capacity of lithium-rich anti-fluorite lithium iron oxide by simultaneous anionic and cationic redox," *Nature Energy*, vol. 2, no. 12, pp. 963–971, 2017.

[20] R. V. Thøgersen, H. H. Hval, and H. Fjellvåg, "Elucidation of the reaction mechanisms in antifluorite-type $Li_{5+x}Fe_{1-x}Co_xO_4$ positive electrodes for Li-ion batteries," *Batteries & Supercaps*, vol. 7, no. 9, p. e202400348, 2024.

[21] C. Zhan, J. Lu, and K. Amine, "Understanding the evolution of the Li-rich antifluorite $Li_5FeO_4$ upon electrochemical delithiation," *ECS Meeting Abstracts*, vol. MA2016-03, no. 2, p. 886, 2016.

[22] O. Toyoki, S. Masahiro, and K. Hironori, "Effect of bulk and surface structural changes in $Li_5FeO_4$ Positive electrodes during first charging on subsequent lithium-ion battery performance,"

*Journal of Materials Chemistry A*, vol. 2, no. 30, pp. 11847–11856, 2014.

[23] L. Trahey, C. S. Johnson, J. T. Vaughey, S.-H. Kang, L. J. Hardwick, S. A. Freunberger, P. G. Bruce, and M. M. Thackeray, "Activated lithium-metal-oxides as catalytic electrodes for Li-$O_2$ Cells," *Electrochemical and Solid-State Letters*, vol. 14, no. 5, pp. A64–A67, 2011.

[24] K. Harada, M. Hibino, H. Kobayashi, Y. Ogasawara, S. Okuoka, K. Yonehara, H. Ono, Y. Sumida, K. Yamaguchi, T. Kudo, and N. Mizuno, "Electrochemical reactions and cathode properties of Fe-doped $Li_2O$ for the hermetically sealed lithium peroxide battery," *Journal of Power Sources*, vol. 322, pp. 49–56, 2016.

[25] W. M. Dose, C. Villa, X. Hu, A. R. Dunlop, M. J. Piernas-Muñoz, V. A. Maroni, S. E. Trask, I. Bloom, V. Dravid, and C.r S. Johnson, "Beneficial effect of $Li_5FeO_4$ lithium source for Li-ion batteries with a layered NMC cathode and Si anode," *Journal of The Electrochemical Society*, vol. 167, no. 16, p. 160543, 2020.

[26] C. Liu, H. Zhang, W. Zhou, X. Tian, T. Zhang, S. Niu, J. Li, M. Cao, Q. Wang, F. Lv, T. Peng, L. Tao, X. Rang, Z. Chen, and X Su, "Air-stable $Li_5FeO_4$ additive enabled by carbon coating for energy-dense lithium-ion batteries," *Nature Communications*, vol. 16, no. 1, p. 7694, 2025.

[27] Z. Zeng, L. Shang, Z. Hu, Z. Wang, X. Xin, and Y. Liu, "$Li_5FeO_4$ @C high capacity prelithium cathode materials for lithium-ion batteries," *Energy Storage Science and Technology*, vol. 14, no. 5, pp. 1875–1883, 2025.

[28] H. Li, and H. Zhou, "Enhancing the performances of Li-ion batteries by carbon-coating: present and future," *Chemical Communications*, vol. 48, no. 9, pp. 1201–1217, 2012.

[29] S. Park, M. You, Y. Byeon, C. Song, S. Oh, J. Kim, and M. Park, "Stabilizing the surface of $Li_2NiO_2$ cathode additive by coating amorphous niobium oxy-carbide for lithium-ion batteries," *Materials Today Energy*, vol. 36, p. 101351, 2023.

[30] R. Yu, M. Jia, J. Liu, H. Zheng, Q. Zhang, H. Yan, C. Li, E. Chen, C. Lin, Y. Chen, Y. Wang, and X. Gao, "Lithium-Rich antifluorite $Li_5Fe_xAl_{1-x}O_4$: Phase-controllable syntheses, local structural evolution, and electrochemical performance," *Inorganic Chemistry,* vol. 65, no. 23, pp. 13144–13152, 2026.

[31] J. Wang, X. Li, K. Zeng, C. Zhao, Z. Wu, and D. Wang, "Crystal structure modification enhances air stability and suppresses $O_2$ evolution in $Li_5FeO_4$: insights from experiments and DFT calculations," *Journal of Materials Chemistry A*, vol. 13, no. 22, pp. 16618–16627, 2025.

[32] B. Zhu, W. Zhang, S. Li, N. Wen, J. Zheng, C. Guan, J. Li, and Z. Zhang, "Lattice modulation on air-stable Fe-based prelithiation materials with high capacity via triggering anionic redox activity," ACS Applied Materials & Interfaces, vol. 17, no. 8, pp. 12448–12457, 2025.

[33] B. Zhu, N. Wen, J. Wang, Q. Wang, J. Zheng, and Z. Zhang, "Defect engineering of air-stable $Li_5FeO_4$ towards an ultra-high capacity cathode prelithiation additive," *Chemical Science*, vol. 15, no. 32, pp. 12879–12888, 2024.

[34] D. Wang, J. Wang, X. Li, C, Han, H. Fei, and Z. Wu, "Enhanced prelithiation performance of $Li_5FeO_4$ cathode additive and optimized solid electrolyte interface enabled by Mn substitution," *Journal of Alloys and Compounds,* vol. 992, p. 174607, 2024.

[35] B. Zhu, W. Zhang, N. Wen, S. Li, J. Zheng, C. Guan, J. Li, and Z. Zhang. "Structurally modulated advanced Na-doped antifluorite- based pre-lithiation reagents towards superior lithium compensation," *Chemical Engineering Journal,* vol. 509, p. 161529, 2025.

[36] N. Wen, J. Li, B. Zhu, J. Guo, and Z. Zhang, "Unraveling the delithiation mechanism of air-stabilized fluorinated lithium iron oxide pre-lithiation material," *Chemical Engineering Journal*, vol. 497, p. 154536, 2024.

[37] H. Kobayashi, Y. Nakamura, M. Nakayama, S. Kodaki, R. Matsuo, and I. Honma, "Metastable cubic structure exceeds capacity limit of antifluorite $Li_5FeO_4$ cathode using small polarized oxygen redox," *Advanced Energy Materials*, vol. 13, no. 9, p. 2203441, 2023.

[38] Y. Lim, D. Kim, J. Lim, J. Kim, J. Yu, Y. Kim, D. Byun, M. Cho, K. Cho, and M. Park, "Anti-fluorite $Li_6CoO_4$ as an alternative lithium source for lithium ion capacitors: An experimental and first principles study," *Journal of Materials Chemistry A*, vol. 3, no. 23, pp. 12377–12385, 2015.

[39] N. Kuganathan, P. Iyngaran, and A. Chroneos, "Lithium diffusion in $Li_5FeO_4$," *Scientific Reports*, vol. 8, no. 1, p. 5832, 2018.

[40] Z. Lin, Z. Tong, H. Cai, C. Li, Y. Ding, C. Lv, and M. Lu, "Prelithiation technology for high energy density lithium-ion batteries: Design, progress, advantages and challenges," *Energy Storage Materials,* vol. 83, p. 104709, 2025.

[41] A. M. Augustine, V. Sudarsanan, and P. Ravindran, "Ti substitution in $Li_5FeO_4$: A Li-rich cathode material for Li-ion batteries from first principles calculations," E*CS Journal of Solid State Science and Technology*, vol. 10, no. 10, p.101006, 2021.

[42] A. M. Augustine, V. Sudarsanan, and P. Ravindran, "Suppressing the initial capacity fade in Li-rich $Li_5FeO_4$ with anionic redox by partial Co substitution – a first-principles study," *Sustainable Energy Fuels*, vol. 7, pp. 1502-1521, 2023.

[43] Z. Tabandeh, F. Zergani, and S. Ghasemi, "Unveiling siliborophene's potential as an anode material for advancing Li ion batteries: DFT and ab-initio molecular dynamics," *Journal of Energy Storage*, vol. 76, p. 109640, 2024.

[44] V. Ásgeirsson, B. Birgisson, R. Bjornsson, U. Becker, F. Neese, C. Riplinger, and H. Jónsson, "Nudged elastic band method for molecular reactions using energy-weighted springs combined with eigenvector following," *Journal of Chemical Theory and Computation*, vol. 17, no. 8, pp. 4929–4945, 2021.

[45] W. Lee, H. Lee, Y. Byeon, J. Kim, W. Choi, M. Choi, M. Park, and W. Yoon, "Modulating anion redox reactions and structural evolution through Fe-substitution in $Li_6CoO_4$ hyper-lithiated sacrificial cathodes," *Advanced Energy Materials*, vol. 13, no. 42, p. 2302316, 2023.

[46] W. Li, G. Wu, C. M. Araújo, R. H. Scheicher, A. Blomqvist, R. Ahuja, Z. Xiong, Y. Feng, and P. Chen, "$Li^+$ ion conductivity and diffusion mechanism in α-$Li_3N$ and β-$Li_3N$," *Energy & Environmental Science*, vol. 3, no. 10, pp. 1524–1530, 2010.

[47] L. Li, E. Lee, J. W. Freeland, T. T. Fister, M. M. Thackeray, and M. K. Y. Chan, "Identifying the chemical origin of oxygen redox activity in Li-rich anti-fluorite lithium iron oxide by experimental and theoretical x-ray absorption spectroscopy," *The Journal of Physical Chemistry Letters*, vol. 10, no. 4, pp. 806–812, 2019.